A DFT+U theoretical study of the effect of aluminum quantities on the structural, electronic, elastic and optic properties of Zinc oxide compound

S. Haireche[a,*], M. Elbaa[b], M. Habireche[a] and M. Bouchenafa[c]

[a]*Laboratory of Mechanics, Physics, and Mathematical Modelling, University of Medea, Medea 26000, Algeria.*
[b]*Department of Material Sciences, Faculty of Sciences and Technology, Djilali Bounaama University of Khemis Miliana, 44225, Algeria.*
[c]*Laboratoire de Matériaux pour Application et Valorisation des Energies Renouvelable (LMAVER), Département de Sciences de la Matière, Université Amar Telidji Laghouat, BP 3000, Algeria.*

Received 10 August 2025; accepted 2 July 2026

This work presents a comprehensive ab initio investigation of the structural, electronic, elastic, and optical properties of aluminum-doped zinc oxide ($Zn_{1-x}Al_xO$) using the DFT+U framework. A realistic $2\times2\times2$ supercell model is employed to simulate substitutional doping at various Al concentrations (up to 25%). The results reveal a systematic reduction in band gap energy, reaching 2.216 eV at the highest doping level, which reflects enhanced electrical conductivity. Density of states analysis highlights the emergence of Al-3p states near the conduction band, contributing to donor-like behavior and supporting n-type conductivity. The elastic properties show a progressive decrease in stiffness and an increase in anisotropy with Al content, indicating mechanical softening of the ZnO matrix. Optically, the doped systems exhibit improved transparency, a blue shift in the absorption edge, and modulation of the dielectric response, consistent with the Burstein Moss effect. These findings suggest that Al doping significantly tailors the multifunctional behavior of ZnO, making it a promising candidate for transparent conducting electrodes, optoelectronic components, and sensor technologies. The theoretical insights presented herein provide useful guidelines for experimental optimization of Al doped ZnO-based materials.

Keywords: GGA+U; $Zn_{1-x}Al_xO$; DFT; gap energy; transmission; supercell.

DOI: https://doi.org/10.31349/RevMexFis.72.060501

1. Introduction

For many years, Zinc oxide has been used in the chemical and pharmaceutical industries [1, 2]. Zinc oxide (ZnO) holds significant potential in the medical field, particularly in drug delivery systems and cancer treatments, due to its biocompatibility, antimicrobial properties, and ability to target cancerous cells effectively [3, 4]. New avenues of research in optoelectronics are beginning to advance with the evolution of technology like photoluminescence applications [5–7]. The latest technological trend shows that zinc oxide doping with transition metals such as Sc, Ti, V, Cr, Mn, Fe, Co, Ni and Cu can be used as a ferromagnetic material and also has great interest in spintronic applications [8–10]. After industrial interest in this material became more prominent, research into its physical properties was extensively studied not only for the development of the microelectronics industry but also to collect as much information as possible on its energy behavior concerning the preparation conditions. ZnO, with its wide gap (3.37 eV) and its high binding energy (60 meV), is considered one of the most promising semiconductor materials for technological applications such as laser diodes emitting in blue and UV spectra [11–13]. Moreover, the thermoelectric field extensively uses ZnO with metallic impurities such as aluminum [14, 15]. Zinc oxide in thin films has enjoyed considerable importance in various fields of research in recent decades due to its multiple potential applications in optoelectronics, such as solar cells [16], spintronics [17–19], gas sensors [20], and photodetector applications [21]. Doping ZnO with suitable elements can improve its optical characteristics with increased transmission in the visible ($T \sim 90\%$) and accelerate the run for its practical applications [22–28]. Also, oxygen vacancies improve both optical and electrical properties, particularly electrical conductivity ($\sigma \sim 10^{-3}\ \Omega^{-1}$ cm^{-1}) [29–32]. Moreover, thermal treatment plays a crucial role in improving the electrical properties of ZnO, as demonstrated by the work of Abdullin *et al*. [33]. Furthermore, sintering and precursor concentration have a greater impact on ZnO physical properties [34]. In particular, the doping of ZnO with Aluminum considerably modifies its physical properties [35–37]. Al-doped ZnO compounds exhibit high transparency in the visible range [38, 39]. It has been shown that the gap can be controlled by introducing a small amount of aluminum [40]. Several research groups are currently working on developing more efficient solar cells by doping zinc oxide with aluminum [41, 42]. For three decades, the number of publications addressing the doping of ZnO has failed to fundamentally understand the effect of doping with metallic elements on electrical, optical, and electronic properties. This work focuses on the microscopic aspect of doping on band gap energy, elasticity, and optical absorption. This study aims to deepen the understanding of the atomic-scale effects of aluminum doping in ZnO, with a focus on its structural and mechanical behavior relevant to advanced technological

applications. By employing a realistic $2 \times 2 \times 2$ supercell model, we sought to closely mimic experimental conditions and generate reliable data on dopant-induced changes. Special emphasis was placed on comparing ZnO:Al with other transparent conducting oxides to assess its standing within this family of materials. The findings help categorize the material based on its directional performance and mechanical stability. They also offer valuable theoretical insights to support high-efficiency experimental design.

2. Computational methods and geometric model

In this study, ab initio calculations are performed using the plane wave method, incorporating the pseudopotential approach within the framework of density functional theory (DFT) [43]. To improve the accuracy of the results, the Generalized Gradient Approximation (GGA) was adopted, specifically using the Perdew-Purke-Ernzerhof (PBE) functional [44]. Simulations are carried out using the CASTEP code, leveraging Vanderbilt pseudopotentials to efficiently model electron-ion interactions [45]. The pseudo-potential of Vanderbilt-type ultra-soft was used to compute the potential seen by the valence electrons [46]. This choice of potential enables the following valence configurations to be used: ($3d^{10}4s^2$) for Zn, ($3s^23p^1$) for Al and ($2s^22p^4$) for O. To improve the description of localized electrons (*e.g.*, Zn 3d), we used the DFT+*U* method formulated by Dudarev *et al*., where the total energy is expressed as [47]:

$$E_{\mathrm{DFT}+U} = E_{\mathrm{DFT}} + \frac{U_{\mathrm{eff}}}{2} \sum_{\sigma} \left[\mathrm{Tr}\left(\rho^{\sigma}\right) - \mathrm{Tr}\left(\rho^{\sigma}\rho^{\sigma}\right) \right], \quad (1)$$

where $U_{\mathrm{eff}} = U - J$ is the effective Hubbard parameter (U : On-site Coulomb interaction and J : Hund's exchange parameter), ρ^{σ} is the occupation matrix for localized orbitals with spin σ, E_{DFT} is the standard DFT energy without corrections and Tr is the Trace of a matrix (sum of diagonal elements). Hubbard corrections are also applied, with optimized values of 5.5 eV for d-electrons and 8.5 eV for p-electrons, in order to improve the treatment of electronic correlation effects. These U values have been widely optimized and reported in the literature [40, 48–50]. Unless otherwise stated, we use GGA+U with U^d for Zn and *Up* for O in the literature validated AZO window seen in the study of Shabani *et al*. [51] and report a *U* sensitivity analysis confirming that all qualitative trends versus Al content are robust. We employ GGA+*U* with the previously cited, in house optimised parameters calibrated to the band gap, Zn(3d) binding energy, and equilibrium *a* and *c*, and no *U* is applied to Al(3p), and the qualitative trends remain robust within $\pm$0.5 eV.

In ab-initio calculation, it is necessary to test the convergence of the results with respect to the cut-off energy ($E^{\text{cut-off}}$) and the K-points mesh configuration in the first Brillouin zone (1BZ). According to the optimization operation, a good convergence is obtained for a plane-wave energy of Ecut-off values of 500 eV and $6 \times 6 \times 4$ K- points mesh configuration. In this study, Al atoms are introduced into the hexagonal wurtzite structure of ZnO via a substitutional doping mechanism. Figure 1 illustrates a 2×2×2 ZnO supercell consisting of 16 zinc and 16 oxygen atoms, designed to allow the systematic substitution of Zn atoms with Al at different doping concentrations. Specifically, Al atoms substitute Zn atoms at atomic ratios of $x = 6.25\%$, 12.5%, 18.75% and 25%, corresponding to 1, 2, 3, and 4 Al atoms, respectively, within the supercell. This method preserves the overall hexagonal symmetry while allowing investigation of the effects of increasing dopant content on the structural and electronic properties of zinc oxide. The substitution of Zn^{2+} with smaller Al^{3+} ions introduces extra free electrons into the system, making it suitable for n-type conductivity enhancement. The supercell approach facilitates accurate modeling of local distortions, charge distribution, and band structure modifications resulting from Al incorporation. Compositions up to 25% Al are modeled in a 2×2×2 supercell to sample defect-defect interactions and provide an upper bound on electronic/elastic trends. This does not assert bulk equilibrium solubility at 25% rather, it reflects non-equilibrium thin film processing windows where high nominal Al contents are reported while wurtzite reflections persist in XRD. Experimental evidence for such regimes (FCM-CVD) and a discussion of possible phase separation at very high Al are provided in the references.

Similar criteria were employed by Damente *et al*., who also selected doping sites to maintain the symmetry of the hexagonal lattice [37]. Other studies, such as those by Jafarova *et al*., have selected the dopant-receiving sites based

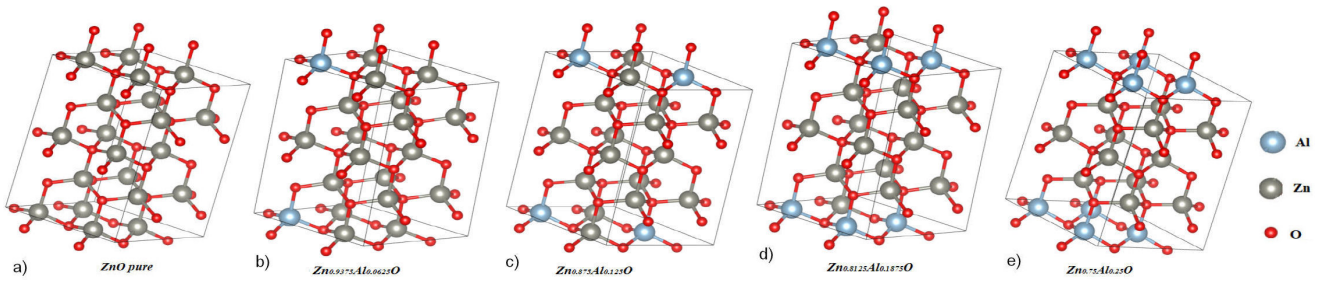


FIGURE 1. 2×2×2) supercell models of a) pure ZnO and Al-doped ZnO with x(%) = Al/Zn: b) 6.25%, c) 12.5%, d) 18.75%, and e) 25%.

TABLE I. Optimised lattice parameters *a* (Å) and *c*(Å), cell volume *V* **(Å^3)** for ZnO compared with other experimental and theoretical results ($\Delta a/a$ and $\Delta c/c$: Relative error without units on the lattice parameters *a* and *c*, respectively).

	$Zn_{1-x}Al_xO$						Reference
Our results	x	a (Å)	$\Delta a/a$ (%)	c (Å)	Δc/(%)	**V(Å^3)**	
	0	3.284	1.64	5.299	2.39	49.491	GGA
	0.0625	3.251		5.294		48.119	
	0.125	3.249		5.205		47.259	
	0.1875	3.268		5.369		57.339	
	0.25	3.172		5.877		59.131	
	0	3.219	0.37	5.184	0.17	46.519	GGA+U
	0.0625	3.249		5.205		47.252	
	0.125	3.188		5.607		49.007	
	0.1875	3.233		5.190		46.653	
	0.25	3.219		5.180		49.088	
Other (Exp.)	0	3.231	-	5.175	-	46.785	[17]
Other (Theo.)	0	3.240	6.93	5.190	0.08	47.183	[54]
		3.340	7.29	5.350	0.58	51.687	[55]
		3.184	10.23	5.147	3.16	45.184	[56]
		2.940	6.85	5.070	0.74	37.952	[57]
		3.225	0.33	5.174	0.27	46.603	[58]
		3.186	6.44	5.150	0.23	45.272	[59]
		3.240	5.15	5.190	0.69	47.183	[60]

on the criterion of minimizing the system's total energy [52, 53]. Finally, self-consistency calculations were considered converged when the system's total energy become stable, ensuring the results' reliability. Graphical representations and crystal structure visualizations are performed using the Origin software and the VESTA applications.

3. Results and discussions

3.1. Structural properties

The first and fundamental step in *ab initio* calculations is the determination of a material's structural properties. This phase is crucial as it provides key insights into the material microstructure, serving as the basis for subsequent calculations related to electronic and elastic properties. The optimized lattice parameters of ZnO are essential for understanding its structure and impact on various physical properties. These parameters offer valuable information about the atomic arrangement within the crystal lattice, ultimately influencing its mechanical, thermal, and electronic behavior. Table I provides an overview of the structural properties, comparing them with existing experimental and theoretical data. To validate our findings, we meticulously compared our optimized values with existing experimental and theoretical data. Our results for the undoped and Al-doped ZnO lattice parameters and volumes are in excellent agreement with the existing experimental and theoretical data. The relative errors in the lattice parameters Δa/a and Δc/c, calculated using DFT-GGA for the undoped ZnO, are 1.64% and 2.39%, respectively. In contrast, the corresponding deviations obtained using the DFT-GGA+U approach are significantly reduced to 0.37% and 0.17%, respectively. These results demonstrate that the inclusion of the Hubbard U correction in the GGA framework enhances the accuracy of the structural predictions and yields better agreement with experimental data.

Within GGA+U, the lattice-parameter response to Al doping results from an interplay of the local chemical pressure shorter Al–O bonds contract AlO^4 tetrahedra followed by anisotropic relaxation through the wurtzite framework and electronic changes Al donor electrons increase screening and ionicity, softening bond-bending and coupling *a*-*c* via the internal coordinate *u*. This balance yields small, composition dependent shifts and non-monotonic features in *a* and *c*, which we attribute to how specific Al configurations in the $2\times2\times2$ supercell redistribute local strain between basal and axial directions.

In DFT, the GGA+U approximation is generally more suitable for the geometric optimization of materials that exhibit strong electronic correlation effects, such as those containing transition elements with *d*-orbitals or *f*-orbitals. The GGA alone may underestimate the band gap and fail to accurately capture strongly correlated electronic interactions. In contrast, adding the U term (Hubbard correction) in GGA+U enhances the description of these interactions by correcting the energy of localized electrons, often leading to more precise geometric optimizations for these types of systems [49, 50]. According to the DFT criteria outlined by Damonte *et al.*, our results exhibit strong agreement with both experimental and theoretical data [37]. For undoped Zinc oxide,

our study yielded a value of 3.219 Å and 5.184 Å for *a* and *c*, aligning closely with theoretical values of 3.225 Å and 5.174 Å [58] and 3.184 Å and 5.147 Å [56]. This result also demonstrated favorable agreement with the experimental values of 3.231 Å and 5.175 Å for *a* and *c*, respectively [20]. In the case of doping, the lattice parameters *a* and *c* of aluminum doped ZnO change only slightly, and the crystal structure approximately retains its hexagonal lattice, despite the absence of experimental values for a proper comparison.

These findings highlight the complexity of crystalline behavior in these compounds and stress the significance of integrating both theoretical and experimental perspectives. This comprehensive comparative study enhances our understanding of the structural properties of both undoped and Al doped ZnO, contributing to the broader knowledge of their unique crystalline behaviors.

3.2. Electronic properties

Band structure of undoped and Al doped ZnO

The band structure is composed of permitted and prohibited energy bands. The permitted energy bands, also called valence and conduction bands, determine the electrical properties of the material. The valence band is the lowest energy band and is generally occupied by electrons. The conduction band is the highest energy band, which can be partially or completely empty. From an energetic point of view, a material band gap corresponds to the lowest energy needed for an electron to transition from the valence band to the conduction band. Materials can be classified based on the size of this bandgap into insulators (large bandgap), semiconductors (medium-sized bandgap), and conductors (zero or near-zero bandgap). The graphs in Figs. 2a) to 2e) represent the band structures of ZnO and Al doped ZnO at various atomic ratios of Al/Zn from 0 to 25% Al impurity quantities. In this graph, the gap energy between the valence and conduction bands is distinctly observable. The Fermi level lies in the middle of the bandgap, indicating it's an intrinsic semiconductor. In the undoped ZnO, the material exhibits a direct band gap located at the Γ point, consistent with the known semiconducting behavior of pure wurtzite ZnO.

As Al is introduced into the ZnO lattice, a systematic reduction in the band gap is observed across the series (b–e), accompanied by a noticeable shift of the conduction band minimum (CBM) toward lower energies, especially near the Γ M points. This narrowing is attributed to the incorporation of Al-3p orbitals, which contribute additional conduction states and introduce donor-like behavior, effectively lowering the CBM.

While the valence band maximum (VBM) remains relatively stable in energy, slight changes in its curvature and dispersion are observed, reflecting the perturbation of the electronic structure due to local lattice distortions and Al–O bonding. The shift is most pronounced at 25% doping, where the band gap becomes significantly reduced and the bands exhibit increased overlap and dispersion, suggesting a transition toward a more conductive regime.

In previous results, it is observed that replacing a certain percentage of zinc with aluminum leads to a decrease in the energy gap as the doping level increases [63]. By comparing our results with the theoretical ones, we see an improvement in the value of the gap for $Zn_{1-x}Al_xO$. K. Dakhsi's study showed that the gap energy of films decreases from 3.29 eV for undoped ZnO to 3.27 eV for 5% Al-doped ZnO [64]. This decrease is attributed to distortions of the crystal lattice caused by the introduction of impurities and the increase in the concentration of free electrons. Additionally, the gap decreases as the concentration of metal doping increases [65]. In contrast, results from FCM-CVD reveal a relatively stable bandgap around 3.1-3.2 eV for doping levels between 0% and

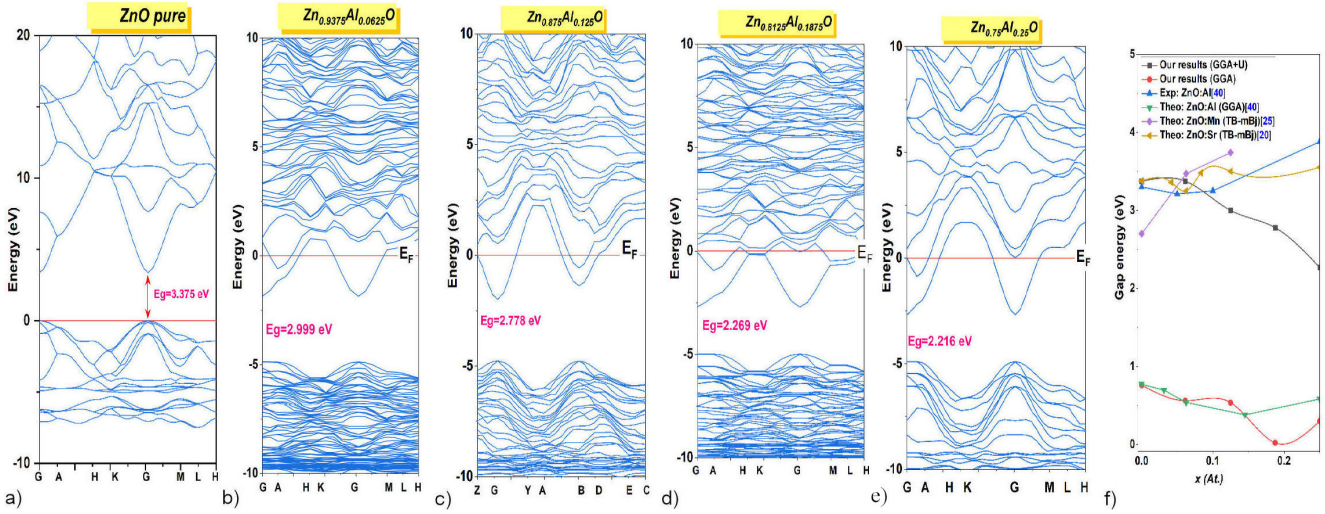


FIGURE 2. Band structure for: a) the undoped ZnO and Al doped ZnO with different atomic ratios of doping b) 6.125%, c) 12.5%, d)18.75% and e) 25%, f) Evolution of the band gap energy as a function of dopant concentration in previous research.

and 5%, indicating limited Al solubility or incorporation under those processing conditions [40]. Figure 2f) illustrates the variation in band gap energy as a function of aluminum doping concentration in ZnO. The trend shows a significant decrease in Eg with increasing Al doping from the undoped ZnO to 25% Al doped ZnO. Initially, for pure ZnO (x = 0), the band gap is around 3.375 eV. As Al is introduced (x = 0, 0.06125, 0.125, 0.1875, 0.25), the band gap decreases, reaching a minimum at $x = 0.25$, dropping to approximately 2.216 eV. This reduction is attributed to introducing free carriers and changes in the electronic structure caused by Al substitution. The observed trend suggests that controlled Al doping allows for tuning ZnO electronic properties, making it suitable for various optoelectronic and transparent conductive applications.

TDOS and PDOS of Undoped and Al doped ZnO

The density of states (DOS) is a fundamental physical quantity that provides deep insights into the electronic band structure of materials. Understanding DOS is essential because it influences many of the material electronic properties, such as electrical conductivity, optical absorption, and thermal properties. By examining the DOS, particularly the total density of states (TDOS) and partial density of states (PDOS), researchers can infer critical information about the distribution of electrons at various energy levels within a material. This understanding is especially important for materials like ZnO, which have widespread applications in electronics and optoelectronics due to their specific properties. Figure 3 shows the Total Density of States (TDOS) and Projected Density of States (PDOS) for both undoped and doped ZnO, with different atomic ratios of x =Al/Zn ($x = 0$, 0.0625, 0.125, 0.1875 and 0.25). Peaks in the PDOS indicate significant contributions from specific orbitals at corresponding energies. In the context of zinc oxide (ZnO), in its pure and aluminum-doped forms, the DOS analysis reveals intricate details about how doping affects the material's electronic structure. Typically, the energy origin in these analyses is fixed at the Fermi level, which serves as a reference point for measuring the energy distribution of electrons. The undoped ZnO is also presented for comparison purposes. The total and partial density of states (TDOS and PDOS) of Al-doped ZnO, evaluated over the energy range from -15 eV to +15 eV, reveal substantial modifications in the electronic structure with increasing Al concentration. In the deep valence region (-15 eV to -5 eV), the PDOS is dominated by oxygen 2s states, showing minimal sensitivity to doping levels. Between -5 eV and 0 eV, the valence band is primarily composed of O-2p states, with a minor contribution from Zn-3d orbitals, which remain relatively stable across different doping ratios. However, as the Al content increases, a slight shift and broadening in this region indicate perturbations in the local bonding environment, particularly due to Al–O interactions. Around the Fermi level (set at 0 eV), the undoped ZnO displays a clear band gap characterized by the absence of electronic states, while the doped structures exhibit a progressive narrowing of this gap. For doping levels starting from 6.25% up to 25%, the conduction band minimum shifts closer to the Fermi level, with Al-3p states contributing significantly to the conduction region just above 0 eV. In some cases, shallow donor states appear within the gap, indicating the possibility of n-type conductivity enhancement. The conduction band (0 to +5 eV) becomes increasingly populated with Al-derived states, which hybridize partially with Zn-4s and O-2p orbitals, suggesting an improved carrier mobility. At higher energies (beyond +5 eV), the contributions of Zn and Al states remain notable but less structured, indicating a convergence toward free-electron-like behavior. Overall, the TDOS and PDOS profiles demonstrate that Al doping modifies both the valence and conduction band edges, introduces new states near the Fermi level, and thus significantly influences the optoelectronic properties of ZnO. Zhou *et al*. obtained similar results in their study on the bonding mechanism of ZnO using the LDA+U method [66]. A detailed analysis of the PDOS for undoped ZnO reveals that the oxygen atom's p orbitals dominate the valence band, contributing more significantly than the zinc atom's s orbitals. The valence band of ZnO is predominantly shaped by the electronic contributions of oxygen atoms, indicating that O-2p orbitals govern the bonding in-

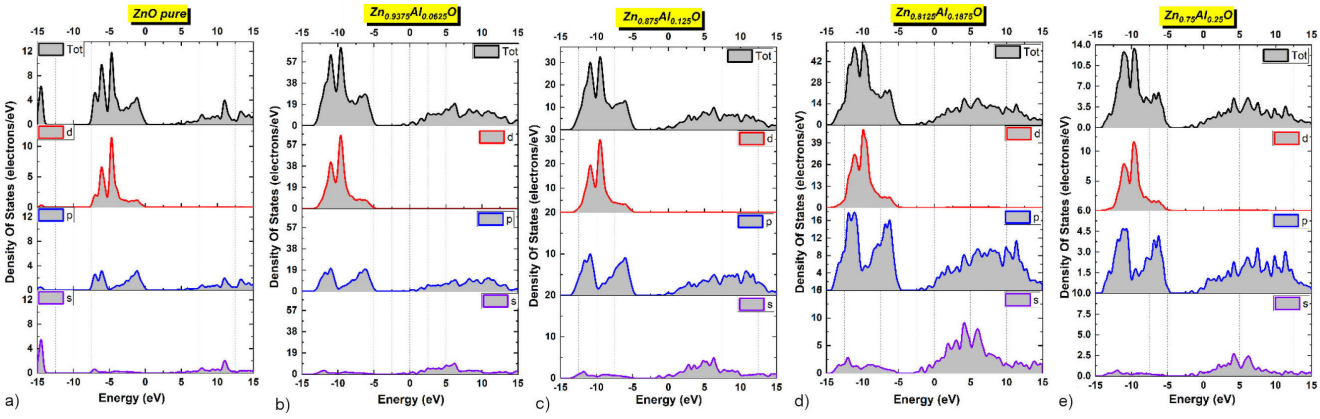


FIGURE 3. TDOS and PDOS for a) undoped ZnO and with different atomic ratios of Al/Zn b) 6.25%, c) 12.5%, d) 18.75% and e)25%.

teractions in this region. In contrast, the conduction band is mainly influenced by the Zn-4s orbitals, which are critical to the material's electrical conductivity [67]. In the case of ZnO doped with 25% Al, the total and partial density of states (TDOS and PDOS) reveal the electronic effects of aluminium incorporation.

Doping with Al alters the electronic structure by shifting energy levels and modifying the intensity and distribution of DOS peaks, thereby impacting the material's electronic and conductive properties [68].

As depicted in Fig. 3, the upper energy states of the doped system are primarily derived from the Zn d-orbitals, O p-orbitals, and Al p-orbitals. A detailed comparison between the PDOS of doped and undoped ZnO highlights pronounced differences, particularly near the valence band maximum, where Zn and O exhibit distinct modifications. The emergence of new electronic states at the valence band edge is attributed to interactions between Al and its nearest-neighbor Zn and O atoms. These findings confirm that Al doping effectively tailors the DOS of ZnO, in agreement with the observations reported by Khuili *et al*. [67].

To quantitatively connect the DOS to the band-structure evolution and the ensuing n-type conductivity, we note the following trends across $x = 0 \rightarrow 0.25$. For undoped ZnO, EF lies within the gap and the TDOS at EF vanishes, consistent with a direct-gap semiconductor. Upon Al substitution ($Al^{+}3 \rightarrow Zn^{+2}$), one excess electron per Al is donated to the conduction manifold. In the PDOS this appears as Al(3p) driven spectral weight that hybridises with Zn(4s) and O(2p) at the conduction band edge. As x increases, these Al(3p) derived states move into and broaden the CBM region, while EF shifts upward toward and at higher x, into the onset of these states. The net effect is a progressive increase of the DOS at near EF (N(E)> 0), which is the electronic signature of donor filling and explains the measured expected rise in n-type conductivity. This DOS evolution is fully consistent with the band structure trends and with optics: the Burstein Moss blue shift observed in $\varepsilon 2$/absorption follows naturally from EF entering low-lying conduction states, which blocks the lowest interband transitions even as the many-body/electrostatic perturbation narrows the fundamental gap in the calculations. Importantly, the PDOS shows no prominent deep mid-gap resonances, indicating that Al acts as a shallow donor rather than introducing compensating traps hence the finite N(EF) and Al(3p)/Zn(4s) character at the CB edge are the microscopic origin of the enhanced n-type transport.

3.3. Elastic properties

A material elastic constants offer crucial information about the types of forces operating within it as well as a connection between its mechanical and dynamic properties. Specifically, they offer insights into the stability and rigidity of materials [69, 70]. The elastic constants C_{ij} are obtained from the second-order derivative of the total energy with respect to strain [71]:

$$C_{ij} = \frac{1}{V}\frac{\partial^2 E_{\rm tot}}{\partial\varepsilon_i \partial\varepsilon_j}, \tag{2}$$

where V is the equilibrium volume of the unit cell, $E_{\rm tot}$ is the total energy, and ε_i, ε_j are the applied strain components.

In Young's notation, $Zn_{1-x}Al_xO$ compounds exhibit a hexagonal crystal structure, with their elasticity tensor comprising five independent components: C^{11}, C_{12}, C_{13}, C_{33} and C_{44} [60].

These constants represent different components of the stiffness tensor, which describe how the material deforms under various stress conditions. Specifically, C^{11} quantifies the stiffness in the direction parallel to the crystallographic axis, indicating the material's resistance to deformation along this axis. C_{12} and C_{13} describe the interactions between perpendicular stress and strain components, providing insight into how the material reacts when stress is applied in one direction but strain occurs in another [72]. C_{33} represents the stiffness along the crystallographic c-axis, which is particularly rele-

TABLE II. Elasticity constants C_{ij} (in GPa) of $Zn_{1-x}Al_xO$ with $x = 0$, 0.0625, 0.125, 0.1875 and 0.25 compounds compared with other theoretical and experimental results.

Elasticity constants C_{ij} (GPa)		C_{11}	C_{12}	C_{13}	C_{33}	C_{44}	Ref.
Our results	ZnO	214.987	114.654	106.872	194.142	34.052	
	$Zn_{0.9375}Al_{0.0625}O$	195.452	92.740	100.840	165.887	18.633	
	$Zn_{0.875}Al_{0.125}O$	183.288	98.143	92.854	172.214	20.547	
	$Zn_{0.8125}Al_{0.1875}O$	170.915	95.190	91.732	140.756	31.805	
	$Zn_{0.75}Al_{0.25}O$	150.193	89.124	98.540	171.232	21.241	
Exp. data	ZnO	206 ± 4	118 ± 10	211 ± 4	44.3 ± 4	44.6 ± 4	[58]
Theo. data	ZnO	293.31	104.24	73.55	278.27	54.63	[54]
		210	121	105.1	210.9	–	[27]
		191.16	111.96	85.63	190.57	36.89	[56]
		222	118	127	215	51	[74]
		199.7	104.3	92.9	192	43.2	[55]
		240	161	135	253	39.5	[59]

TABLE III. Mechanical properties of Zn1-xAlxO compounds for varying compositions x (x=0, 0.0625, 0.125, 0.1875 and 0.25).

Mechanical	properties		of	$Zn_{1-x}Al_xO$	
x	0	0.0625	0.125	0.1875	0.25
Bulk modulus B (GPa)	142.32	135.80	127.74	118.03	117.80
shear-modulus μ (GPa)	43.369	41.881	36.509	36.149	33.250
Lame λ (GPa)	113.41	109.00	103.40	99.68	95.64
Young modulus E (GPa)	118.11	112.99	100.00	94.17	91.17
Poisson ratio ν	0.362	0.365	0.369	0.368	0.371
Compressibility $\beta.10^{-3}$ (GPa^{-1})	7.06	7.54	7.830	8.05	8.54
Universal anisotropy index A^U	0.181	0.214	0.059	0.698	0.867
Hardness H (GPa)	3.436	3.228	2.828	2.667	2.610

vant for hexagonal materials like ZnO, which have distinct properties along this axis. Finally, C_{55} and C_{66} are the shear moduli, describing the material's resistance to shear deformation. This is crucial for understanding how the material behaves under forces that cause sliding or twisting. The C_{11}, C_{12}, C_{13}, C_{33}, and C_{44} elastic constants of undoped ZnO and Al-doped ZnO are reported in Table II for $Zn_{1-x}Al_xO$ compounds, comparing our results with experimental data and results from other theoretical methods. The mechanical stability of a solid is one of the most crucial characteristics to be inferred from its elastic properties. The mechanical strength of the crystalline lattice was initially formulated by Born and Huang, who demonstrated that stability criteria can be derived based on conditions imposed on the elastic constants, assuming that the internal energy of a crystal remains positive under small deformations. For the hexagonal system, these criteria are given by the following relations of Born and Kuang [73]:

$$C_{11} > |C_{12}, \quad 2C_{13}^2 < C_{33}\left(C_{11} + C_{12}\right), \\ C_{44} > 0, \quad C_{66} > 0. \tag{3}$$

The elastic constants C_{ij} obtained for $Zn_{1-x}Al_xO$ reveal a clear decrease in overall mechanical stiffness as the aluminum doping concentration increases. The progressive reduction of C^{11} (from 214.99 to 150.19 GPa) and C^{33} (from 194.14 to 171.23 GPa) indicates a weakening of the crystal bonding both within the basal plane and along the c-axis. The sharp drop in C^{44} at low doping levels, followed by moderate fluctuations, highlights a pronounced sensitivity to shear deformation. Although less systematic, the changes in C^12 and C^{13} also reflect a gradual disturbance in transverse elasticity caused by the substitution of $Zn^{+}2$ with $Al^{+}3$. Compared to experimental data and other theoretical works, the values remain consistent while capturing the specific effects of the GGA+U method and the use of a supercell model. Overall, the results point to increased mechanical anisotropy and reduced structural robustness with doping, which must be carefully considered when selecting optimal Al concentrations for TCO-based device applications.

Our study determined the elastic constants for $Zn_{1-x}Al_xO$ compounds, with results such as $C_{11} = 191.8$ GPa and $C_{33} = 193.4$ GPa. These values are compared with experimental data from reference [74], where the experimentally measured elastic constants for C_{11} and C_{33} are 206 GPa and 211 GPa, respectively, both with an uncertainty of $\pm$4GPa. Other theoretical methods and calculations, such as PBE-GGA Tb-mBJ and PBE-GGA+U, provide further comparisons. For instance, PBE-GGA Tb-mBJ from references [60, 73] reports C^{11} = 293.31 GPa and C_{33} = 278.27 GPa, demonstrating the variations in results based on different computational methods. Including methods like LDA+U and PBE-GGA+U helps to explore the impact of Coulomb interactions on the material's elastic properties. Table III reports the calculated mechanical properties of $Zn_{1-x}Al_xO$ compounds for varying aluminum concentrations (x=0, 0.0625, 0.125, 0.1875, and 0.25). The results reveal a clear trend of decreasing mechanical strength with increasing Al content, indicating that aluminum incorporation gradually softens the ZnO matrix.

Specifically, the bulk modulus, which reflects the material's resistance to uniform compression, decreases from 142.3 GPa (pure ZnO) to 117.8 GPa at x=0.25, suggesting reduced volumetric stiffness. Similarly, the shear modulus and Young's modulus indicators of resistance to shape change and uniaxial stress, respectively, also exhibit a consistent decline, confirming the weakening of mechanical rigidity upon doping. For instance, the shear modulus drops from 43.4 GPa to 33.3 GPa, and Young's modulus declines from 118.1 GPa to 91.2 GPa. Poisson's ratio slightly increases with doping, from 0.362 to 0.371, implying a more ductile behavior at higher Al concentrations. This is further supported by the Lame parameter, which also decreases, and the compressibility, which increases with doping, indicating enhanced deformability under pressure. A significant observation is the sharp rise in the universal anisotropy index, from 0.181 for undoped ZnO to 0.867 at $x = 0.25$. This indicates increasing elastic anisotropy as aluminum is introduced, likely due to lattice distortion and local inhomogeneity caused by the size and charge differences between Zn^{+2} and Al^{+3} ions. Fi-

nally, the Vickers hardness decreases from 3.44 GPa (ZnO) to 2.61 GPa at the highest doping level, confirming a drop in mechanical hardness with Al incorporation.

Physically, the mechanical softening upon Al substitution arises from a combination of electronic and bonding effects. First, Al acts as a donor, and the added free carriers enhance screening of long-range Coulomb interactions that dominate stiffness in polar wurtzite lattices, thereby reducing the effective interatomic force constants. Second, replacing Zn (whose filled 3d states contribute to Zn(3d)/O(2p) hybridization) with Al (lacking 3d) increases bond ionicity and diminishes directional covalency; this selectively weakens bond bending responses and explains the pronounced reduction in shear-related constants (C_{44}) and the drop in G. Third, the size/charge mismatch (Al^{+3} vs Zn^{+2}) introduces local strain fields and heterogeneity, which elevate elastic anisotropy and open softer deformation pathways. These mechanisms rationalize our computed trends C_{11} and C_{33} decrease with x, B, G, and E decline, Vickers hardness is reduced, and the universal anisotropy index increases indicating a transition toward a more compliant yet still Born stable lattice as Al content rises.

3.4. Optical properties

The study of optical properties of solid materials, including phenomena like absorption, reflection, transmission, and so on, is a basic means of understanding the properties of the materials under the influence of incident light beams. Furthermore, the bandgap of the materials directly affects several optical characteristics, including the absorption coefficient and refraction. The optical properties of materials can be characterized by the transverse dielectric function, represented as $\varepsilon(\omega)$ or complex refractive index *N*, which is expressed as $\varepsilon(\omega) = \varepsilon_1(\omega) + i\varepsilon_2(\omega)$. This function is a fundamental parameter in describing how a material interacts with incident photons across different energy or frequency ranges [38, 43]. The ε_2 is obtained by summing the jumps from occupied to unoccupied states within the selection rule of the Brillouin zone Eq. (1). ε_2 yields ε_1 are calculated from the Kramers-Kronig relationship Eq. (4), and ε_1 is related to the electron polarization rate of the material. The imaginary part of the dielectric function ε_2, is determined by summing the transitions from occupied to unoccupied states, following the selection rules within the Brillouin zone Eq. (4). The real part, ε_1 is then derived from ε_2 using the Kramers-Kronig relation Eq. (5), where ε_1 corresponds to the electron polarization rate of the material [75]:

$$\varepsilon_2(\omega)\left(\frac{4\pi^2e^2}{m^2\omega^2}\right)\sum_{ij}\int|\langle i|M|j\rangle|^2 f_i(1-f_i) \times \delta(E_f - E_i - \omega), d^3k. \quad (4)$$

$$\varepsilon_1(\omega)1 + \frac{2}{\pi}P\int_0^\infty \frac{\omega'\varepsilon_2(\omega')}{\omega'^2-\omega^2}, d\omega'. \quad (5)$$

The real part, $\varepsilon_1(\omega)$, quantifies the amount of electromagnetic wave energy stored as potential energy within the material. In contrast, the imaginary part, $\varepsilon_2(\omega)$, indicates the energy absorbed and dissipated as heat. The refractive index n(ω), the extinction coefficient $k(\omega)$ the absorption coefficient $\alpha(\omega)$, reflectivity $R(\omega)$ and loss function $L(\omega)$ are calculated using the following equations Eqs. (6)-(10) of undoped and Al doped zinc oxide are calculated using the following equations [56]:

$$n(\omega) = \left[\frac{\varepsilon_1(\omega)}{2} + \frac{\sqrt{\varepsilon_1^2(\omega)+\varepsilon_2^2(\omega)}}{2}\right]^{\frac{1}{2}}, \quad (6)$$

$$n(\omega) = \frac{\omega}{c}\sqrt{\frac{\varepsilon_2(\omega)}{2}}, \quad (7)$$

$$\alpha(\omega) = \sqrt{2}\,\omega\left[\sqrt{\varepsilon_1^2(\omega)+\varepsilon_2^2(\omega)} - \varepsilon_1(\omega)\right]^{\frac{1}{2}}, \quad (8)$$

$$R(\omega) = \left|\frac{\sqrt{\varepsilon_1(\omega)+j\varepsilon_2(\omega)}-1}{\sqrt{\varepsilon_1(\omega)+j\varepsilon_2(\omega)}+1}\right|^2, \quad (9)$$

$$L(\omega) = \frac{\varepsilon_2(\omega)}{\varepsilon_1^2(\omega)+\varepsilon_2^2(\omega)}. \quad (10)$$

Figure 4 illustrates the complete set of optical properties of Al doped ZnO for aluminum concentrations ranging from 0% to 25%. The spectral analysis of the optical response reveals pronounced changes in the dielectric behavior, refractive index, optical conductivity, and absorption coefficient, all evolving consistently with increasing Al content ($x = 0$, 0.0625, 0.125, 0.1875, and 0.25).

The real $\varepsilon_1(\omega)$ and imaginary $\varepsilon_2(\omega)$ components of the complex dielectric function, shown in Fig. 4a), serve as primary indicators of electronic polarizability and absorption mechanisms, respectively. In undoped ZnO ($x = 0$), ε_1 exhibits a prominent peak around 3 eV, followed by a gradual decline, indicating strong interband polarization and moderate dispersion. Upon Al incorporation, this peak shifts toward higher photon energies and its magnitude decreases progressively, suggesting enhanced electronic screening and reduced static polarization.

Simultaneously, the ε_2 component displays a distinct absorption edge corresponding to the fundamental bandgap of ZnO. As the Al concentration increases, this absorption edge undergoes a blue shift, indicating an apparent widening of the optical bandgap. This shift is attributed to the Burstein Moss effect, wherein the increased carrier concentration fills the lower conduction band states, thereby raising the onset energy of optical transitions.

The static permittivity (ε_1 at zero frequency) decreases as Al doping increases, reflecting a reduced polarization response under low electric fields. This trend is consistent with findings from the studies of Almeida, Rosely [76] and Haireche [77], although contrary results have been reported by Issam Derkaoui [23]. The refractive-index (n) response in

Fig. 4b) similarly confirms the trend. In pure ZnO, the refractive index starts at a relatively high static value (~ 2.1) in the low-energy limit and decreases monotonically with increasing photon energy. As the doping level increases, the peak value of n diminishes, and the overall curve flattens slightly, suggesting that the material becomes optically less dense and more transparent in the visible region. This behavior is consistent with a reduced dielectric constant and increased free carrier contribution.

In some phases, the refractive index stabilizes at high doping levels, indicating that the material becomes less sensitive to further increases in Al concentration. Our results represent an advancement over the study conducted by Dada and Mochena [78]. As depicted in Fig. 4c), the optical conductivity (photon-induced current response) rises sharply across the near-UV ($\sim 3-6$ eV), consistent with dominant interband transitions. While the undoped ZnO shows a sharp onset of conductivity just after the band gap, the doped compounds demonstrate a shift of this onset toward higher energies, along with a broadening of the spectral width and intensity. This again confirms the widening of the optical band gap and suggests increased participation of free carriers due to Al-induced doping. The spectra of the absorption coefficient in Fig. 4d) provide a particularly clear readout of doping effects on light matter interactions. For undoped ZnO, the onset of absorption occurs just above 3 eV, in agreement with the band structure results. As the Al content increases, the absorption edge shifts significantly to higher energies another manifestation of the Burstein Moss shift. Moreover, the intensity of the absorption peaks also varies, reflecting changes in the joint density of states and transition matrix elements. Notably, at higher Al concentrations, a secondary absorption feature appears at higher energies ($\sim 8-10$ eV), likely related to deeper interband transitions involving Zn-3d or Al-3p states. The optical absorption coefficient is a crucial parameter in determining the shape of a solar cell's spectral response curve [79]. The absorption spectrum ranges from 0 eV to 40 eV. Since chalcogenide materials hold great potential for photovoltaic applications, examining the optical absorption spectra under different doping levels is crucial for enhancing their optoelectronic performance [80]. The reflectivity spectra in Fig. 4e) further corroborate these trends: undoped ZnO shows a characteristic semiconductor response with a modest UV peak of $\sim 10-12\%$. With increasing Al doping, the reflectivity in the visible and Near-UV regions slightly decreases, suggesting improved anti-reflective properties and enhanced transmittance desirable for optoelectronic and transparent conducting applications. Reflectivity

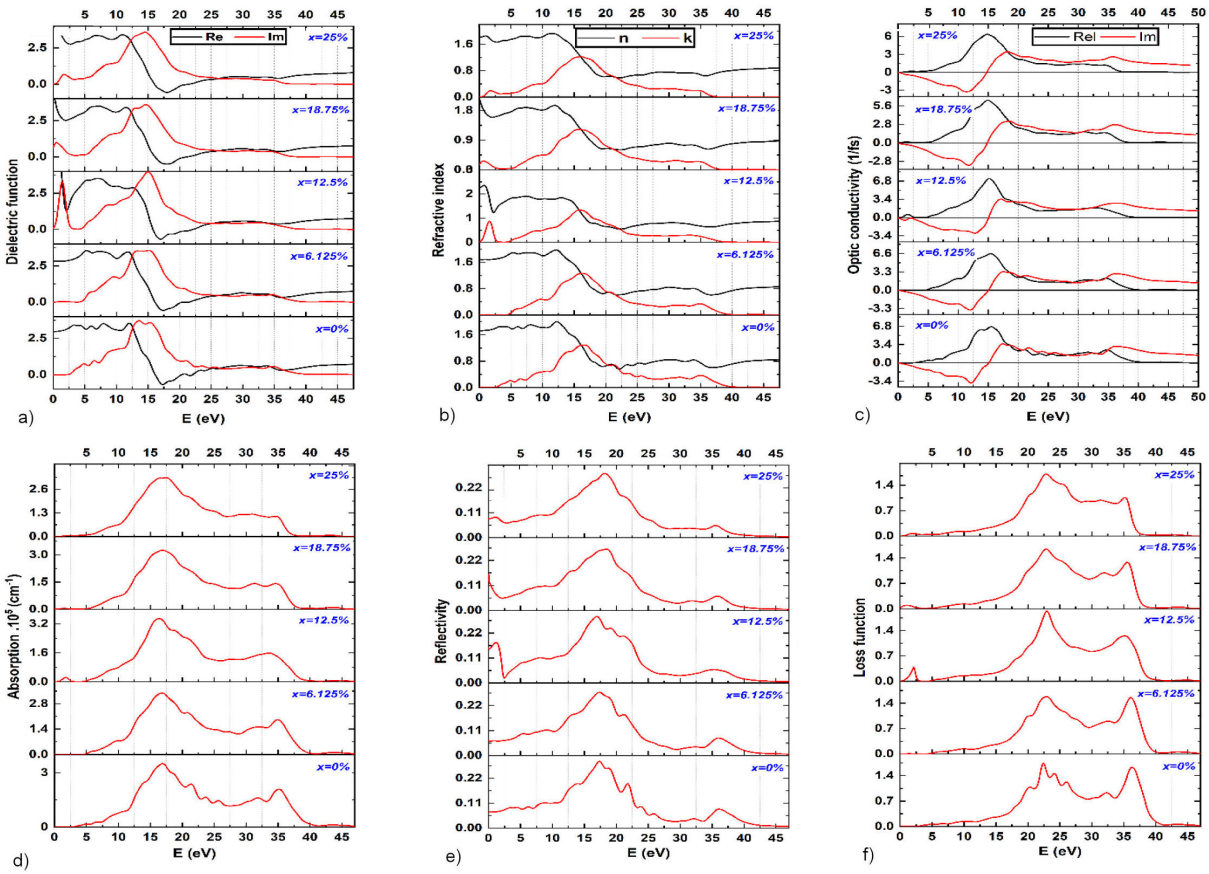


FIGURE 4. Optic properties as a function of energy for $Zn_{1-x}Al_xO$ compounds with $x = 0$, 0.0625, 0.125, 0.1875 and 0.25. a) Dielectric function ε_1 and ε_2 b), refractive index c), optical conductivity, d) Absorption, e) Reflectivity f) Loss function.

TABLE IV. The static absorption coefficient, reflectivity, loss function and gap energy for undoped and Al doped ZnO. $^{(*)}$ band gap calculated with Tauc's method.

x	$\alpha_0.10^{-6}$ cm^{-1}	R_0	n_0	$F_0.10^{-3}$	E_g (eV)	E_g (eV)$^{(*)}$
0	0.0	0.070	1.72	0.00	3.375	3.382
0.0625	0.6	0.064	1.67	0.14	2.999	3.102
0.125	27.2	0.152	2.28	2.84	2.778	3.532
0.1875	226.0	0.157	2.31	22.7	2.269	2.759
0.25	234.0	0.083	1.81	0.48	2.216	2.525

measures the percentage of light reflected off the material's surface rather than being absorbed or transmitted. A notable aspect is the slight shift observed in the reflectivity spectra as the incident photon energy nears the band gap energy, emphasizing the material's responsiveness to specific energy ranges [81]. Lastly, the energy loss function, which characterizes the energy loss of fast electrons traversing the material and is directly linked to the plasmonic behavior, shows a sharp peak in undoped ZnO around 11 eV. This feature is attributed to the collective oscillation of electrons (bulk plasmons). As Al concentration rises, the position of this loss peak shifts slightly toward higher energies, and its intensity increases, indicating a higher carrier density and modified plasmon frequency due to Al-induced free electrons. This plasmonic tunability could be leveraged in advanced photonic applications. The inelastic interaction of electrons with a material is strongly linked to the energy loss function, which defines the likelihood of inelastic scattering, the energy loss distribution, and the angular scattering distribution [46]. The energy loss spectrum illustrates the energy lost by a fast electron as it traverses the material, as shown in Fig. 4f). Peaks in the loss function usually indicate strong plasmonic excitations or other electron excitation phenomena. A weak peak is observed at 37.5 eV, followed by a maximum energy loss of around 22 eV, which coincides with a sharp decline in reflectivity [82]. In the general case, these optical spectra demonstrate that Al doping not only modulates the band structure but also leads to significant tunability in dielectric response, transparency, light absorption, and carrier-induced optical transitions. Such tunability reinforces the potential of Al doped ZnO for applications in transparent electrodes, UV photodetectors, plasmonic devices, and optoelectronic components operating in the UV-visible region.

For band gap estimation, a widely adopted approach relies on analyzing the optical absorption spectra of semiconductors. This method is applicable to materials exhibiting either direct or indirect allowed electronic transitions and is commonly expressed by the following relation [83].

$$(\alpha h\nu)^n = A\,(h\nu - E_g)\,, \tag{11}$$

where α is the absorption coefficient, $h\nu$ is the photon energy, E_g is the optical band gap, A is a constant, and n depends on the nature of the electronic transition: $n = 2$ for direct allowed transitions (as in ZnO), and $n = 1/2$ for indirect ones.

To determine gap energy E_g, one plots $(\alpha.h\nu)^2$ versus $h\nu$ and extrapolates the linear region of the curve to intersect the energy axis. The intercept gives the value of the band gap. This method allows for a simple graphical evaluation of band gap changes due to doping, strain, or defects, and is extensively used in optical characterization of semiconducting thin films and nanomaterials. The Tauc plots presented in Fig. 5 are used to estimate the optical band gap of Al doped ZnO by analyzing the absorption spectra. With increasing aluminum concentration, a clear blue shift in the absorption edge is observed, indicating a progressive widening of the optical band gap. This shift is mainly attributed to the Burstein Moss effect, where additional electrons from Al doping raise the Fermi level, filling low-energy conduction band states and

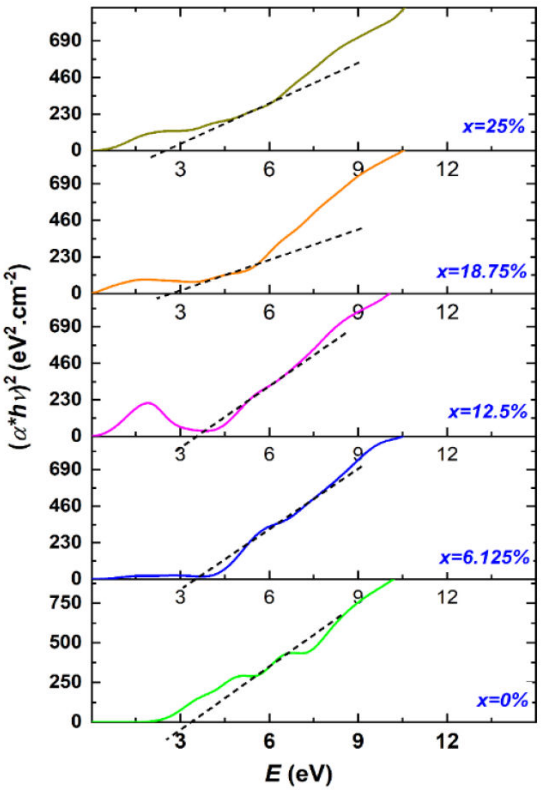


FIGURE 5. Optical band gap estimation by extrapolating the linear region of $(\alpha.h\nu)^2$ versus photon energy $(h\nu)$ plot. The intercept on the energy axis indicates the optical band gap of the $Zn_{1-x}Al_xO$ material.

requiring higher photon energies for electronic transitions. As a result, the band gap decreases from ~ 3.3 eV for undoped ZnO to ~ 2.5 eV at high doping levels ($x = 0.25$). The observed reduction in band gap suggests that doping induces significant modifications in the electronic structure of ZnO, which may enhance its absorption in the visible range but at the expense of its UV selectivity.

Table IV summarises the static optical properties of both undoped and Al-doped ZnO, including the absorption coefficient (α_0), reflectivity (R_0), refractive index (n_0), energy loss function (F_0), and optical band gap energy (Eg), obtained through direct calculation and extrapolation from absorption spectra. In the undoped state, ZnO exhibits negligible absorption at zero frequency, consistent with its known transparency and wide band gap. As the doping concentration increases, particularly beyond $x = 0.125$, the absorption coefficient rises significantly, suggesting the introduction of localised states within the band gap that enable additional optical transitions. Reflectivity initially decreases slightly with low doping levels, then increases at higher concentrations, which may reflect changes in free carrier concentration or dielectric behavior. The refractive index follows a similar nonlinear trend, reaching a maximum at $x = 0.1875$, indicating a stronger polarization response of the material under static fields.

The non-monotonic evolution of the static refractive index n_0 with Al doping (maximum at $x = 0.1875$) reflects a balance between the Burstein Moss shift which raises the apparent optical gap and tends to lower the bound electron polarizability and a concomitant increase in low-energy oscillator strength due to band structure renormalization and spectral weight transfer, which raise $\varepsilon 1(0)$ and n_0. In our dataset, n_0 slightly decreases at very low Al content, then increases to a maximum at $x = 0.1875$ alongside marked rises in A0 and F0, before dropping at $x = 0.25$ as free carrier screening and local field effects reduce the bound polarizability. This interpretation is consistent with classical polarizability relationships and with the joint evolution of R0, A0, F0, and Eg summarized in Table IV.

A sharp increase in the energy loss function is observed at the same concentration, highlighting enhanced plasmonic interactions or collective electron oscillations induced by higher doping. The optical band gap shows a decreasing trend as doping increases, shifting from 3.375 eV in the undoped sample to 2.216 eV at x = 0.25, which can be attributed to band tailing and the incorporation of impurity states despite the potential presence of the Burstein Moss effect. The band gap values obtained via the Tauc method are generally slightly higher than the directly calculated ones, which may be due to the extrapolation assumptions inherent to this method. Overall, these results confirm that aluminum doping significantly modifies the optical response of ZnO, making it a tunable material for applications in optoelectronics and transparent conductive devices.

4. Conclusion

In this work, a detailed first-principles investigation based on the DFT+U formalism was conducted to examine the structural, electronic, elastic, and optical properties of Al doped ZnO. The results demonstrate that aluminum substitution at Zn sites induces measurable variations in lattice parameters while preserving the wurtzite hexagonal symmetry. The electronic structure reveals a systematic narrowing of the band gap with increasing Al concentration, reaching 2.216 eV at 25% doping, highlighting the effectiveness of Al as an n-type dopant. The emergence of Al-3p states near the conduction band enhances electronic conductivity and introduces donor-like behavior. Elastic property analysis confirms a gradual reduction in mechanical stiffness and a rise in anisotropy, suggesting a trade-off between electronic tunability and structural robustness at higher doping levels. Optical characterization reveals substantial modulation of the dielectric function, refractive index, absorption edge, and energy loss spectra, driven by both the Burstein–Moss effect and the formation of impurity states. The improved optical transparency and tunable electronic properties position Al doped ZnO as a strong candidate for applications in transparent conductive oxides (TCOs), UV photodetectors, and optoelectronic devices. The use of a 2×2×2 supercell model allows for a realistic depiction of local atomic distortions and supports the reliability of the predicted trends. These findings offer valuable insights for the design and optimization of Al doped ZnO materials, particularly for photovoltaic, sensing, and biomedical applications. Future work may explore the impact of temperature, defects, and co-doping strategies, as well as experimental validation of the proposed theoretical framework.

Acknowledgments

The authors thank Pr A. El Hdiy (ITheMM/EA7548), Université de Reims Champagne-Ardenne, Reims, France, for valuable discussions. This work was supported by the Algerian Ministry of Higher Education and Scientific Research (MESRS) and the General Directorate of Scientific Research and Technological Development (DGRSDT).

1. C. Shipra, M. Satyabrata, Efficient photocatalytic degradation of antibiotic levofloxacin and organic pollutants in water by Pr doped ZnO nanorods. *Chemical Physics Impact* **9** (2024) 100687, https://doi.org/10.1016/j.chphi.2024.100687

2. A. F. Abdulrahman, A. N. Abdulqodus, M. A. Almessiere, Biosynthesis of Al-doped ZnO nanoparticles with different Al doping ratio for methylene orange dye degradation activity.

Ceramics International **49** (2023) A:34920-34936, https://doi.org/10.1016/j.ceramint.2023.08.165

3. Y. Slimani, S. Caliskan, F. A. Khan, A. Baykal, Anti-cancer activity and optoelectronic properties via DFT calculations of rare-earth dually doped wurtzite-type ZnO nano-systems. *Nano-Structures & Nano-Objects* **40** (2024) 101348, https://doi.org/10.1016/j.nanoso.2024.101348
4. H. R. Abd El-Mageed, Zinc oxide nanoclusters and nanoparticles as a drug carrier for cisplatin and nedaplatin anti-cancer drugs, insights from DFT methods and MC simulation. *Molecular Physics* (2020) e1842533, https://doi.org/10.1080/00268976.2020.1842533
5. P. Latthiwan, P. Sikam, P. Moontragoon, R. Klinkla, A. Watcharapasorn, T. Hussain, T. Kaewmaraya, Controllable terahertz intersubband absorptions in ZnO/(Sb,N) co-doped ZnO quantum wells: First-principles study. *Journal of Physics and Chemistry of Solids* **185** (2024) 111765, https://doi.org/10.1016/j.jpcs.2023.111765
6. I. Musa, R. Faqi, Structural, electrostatic force microscopy, work function, and optical characterization of pure and Al-doped ZnO nanoparticles. *Results in Materials* **22** (2024) 100570, https://doi.org/10.1016/j.rinma.2024.100570
7. U. Jinendra, D. Bilehal, B. M. Nagabhushana, A. P. Kumar, M. Afzal, C. Shivamallu, M. S. Sanjay, S. P. Kollur, Synthesis, characterization, and photoluminescence investigations of Al/Co-doped ZnO nanopowder. *Journal of Molecular Structure* **1305** (2024) 137701, https://doi.org/10.1016/j.molstruc.2024.137701
8. F. Pan, C. Song, X. J. Liu, Y. C. Yang, F. Zeng, Ferromagnetism and possible application in spintronics of transition-metal-doped ZnO films. *Materials Science and Engineering R: Reports* **62** (2008) 1-35, https://doi.org/10.1016/j.mser.2008.04.002
9. Vusala Nabi Jafarova, High Curie temperature and half-metallic ferromagnetism in Cr- and V-doped ZnSe in wurtzite phase: First-principles study, *Solid State Communications*, **369** (2023) 115197, https://doi.org/10.1016/j.ssc.2023.115197.
10. Vusala Nabi Jafarova, Sevda Sabir Rzayeva, First-principles prediction of higher Curie temperature, metallic and half-metallic ferromagnetism in Zn1-x(Vx,Nix)O systems. *Chinese Journal of Physics* **87** (2024) 592-607, https://doi.org/10.1016/j.cjph.2023.11.022
11. A. S. Javaid, W. S. Javaid, M. Adnan, M. Usman, M. A. Akram, N. Bashir, A. Khalid, A. Pervaiz, M. M. Hossin, I. Liaqat, M. A. Ismail, H. Dib, N. Arshad, Synthesis and characterization of efficient Sr-doped ZnO nanostructures for optoelectronic and photocatalytic applications. *Inorganic Chemistry Communications* **162** (2024) 112175, https://doi.org/10.1016/j.inoche.2024.112175
12. X. Huang, S. Chen, J. Pan, Z. Wei, X. Ye, Q. Wang,L. A. Ma, Field emission properties of LIG/ZnO heterojunction prepared by ultrafast laser direct writing. *Ceramics International* **50** 13 Part B (2024) 24205-24216, https://doi.org/10.1016/j.ceramint.2024.04.152
13. S. Jessadaluk, N. Khemasiri, P. Rattanawarinchai, N. Kayunkid, S. Rahong, A. Rangkasikorn, S. Wirunchit, A. Klamchuen, J. Nukeaw, Electroreflectance study of antimony doped ZnO thin films grown by pulsed laser deposition. *Optical Materials* **120** (2001) 111461, https://doi.org/10.1016/j.optmat.2021.111461
14. S. Jantrasee, S. Pinitsoontorn, P. Moontragoon, *journal of electronic materials* **43** (2014) 1689, https://doi.org/10.1007/s11664-013-2834-2
15. U. Ur Rehman, K. Ul Sahar, O. Cherniushok, K. T. Wojciechowski, C. Wang, Wedge-shape Al and Mg co-doped zinc oxide thin films: A Facile Route to achieve high thermoelectric power factor. *Ceramics International* **50** 19 Part B (2024) 36394-36401, https://doi.org/10.1016/j.ceramint.2024.07.022
16. H. Benali, B. Hartiti, F. Lmai, A. Batan, S. Fadili, P. Thevenin, Synthesis and characterization of Al-doped ZnO thin-films for photovoltaic applications. Materials Today: Proceedings (2024) In Press Corrected Proof, https://doi.org/10.1016/j.matpr.2024.06.012.
17. E. B. Buzok, S. Yalcin, G. Demircan, D. Yılmaz, B. Aktas, and E. Aytar, The structural, optical, electrical and radiation shielding properties of Co-doped ZnO thin films. *Radiation Physics and Chemistry* **222** (2024) 111840, https://doi.org/10.1016/j.radphyschem.2024.111840.
18. V. N. Jafarova, U. S. Abdurahmanova and S. S. Rzayeva, Ab initio prediction of half-metallic and metallic ferromagnetism in ZnO:(Co,Cr) systems. *Phys. Scr.* **99** (2024) 065927, https://doi.org/10.1088/1402-4896/ad43a1.
19. V. N. Jafarova, G. S. Orudzhev, S. S. Huseynova et al, Magnetic Properties of Vacancies and Doped Chromium in a ZnO Crystal. *Semiconductors* **52** (2018) 1047-1050, https://doi.org/10.1134/S1063782618080055
20. R. Bhattarai, R. B. Thapa, D. D. Mulmi, R. R. Ghimire, Fabrication of alcohol sensor using undoped and Al doped ZnO nanostructure film with polymer electrolyte gating. *Heliyon*, **10** (2024) e32281, https://doi.org/10.1016/j.heliyon.2024.e32281
21. S. Tekin, B. U. Begum Abdioglu, Er. I. Karaduman, S. Acar, Performance evaluation of SILAR deposited Rb-Doped ZnO thin films for photodetector applications. *J Sol-Gel Sci* **111** (2024) 891-908 https://doi.org/10.1007/s10971-024-06493-8
22. A. Virdian, S. Muhammady, A. M. Naradipa, R. Widita, A. Rusydi, Y. Darma, Enhancing photon absorption and conductivity of ZnO film by Fe doping: Experimental and first-principle perspectives. *Ceramics International* **46** 17 (2020) 27110-27118, https://doi.org/10.1016/j.ceramint.2020.07.188
23. I. Derkaoui, M. Achehboune, I. Boukhoubza, E. El Allam, Z. El Adnani, L. Henrard, A. Rezzouk, Effect of strontium (Sr) doping on the structural, electronic and optical properties of ZnO, by first-principles calculations. *Physica B Condensed Matter* **660** (2023) 414903, https://doi.org/10.1016/j.physb.2023.414903
24. Y. Liu, S. Jiang, X. Zhou, C. Xia, Q. Wu, X. Ma, L. Chen, J. Yao, J. Xu, High-concentration F-incorporated ZnO thin films doped via femtosecond-laser hyperdoping. *Surfaces and Interfaces* **42** Part A (2023) 103367, https://doi.org/10.1016/j.surfin.2023.103367

25. A. Slassi, Physical properties of Mo-doped ZnO by first principles and Boltzmann equations. *Opt Quant Electron* **47** (2015) 2465-2477, https://doi.org/10.1007/s11082-015-0131-4

26. Y. Miao, H. Wang, H. Li, K. He, Q. Wang, The GGA+U method studied the effects of Cu doping on the formation energy, electronic and optical properties of V-doped ZnO. *Opt Quant Electron* **49** (2017) 286, https://doi.org/10.1007/s11082-017-1128-y

27. L. Qiao, C. Chai, Y. Yang, X. Yu, C. Shi, First-principles theoretical study on band of strained wurtzite Nb-doped ZnO. *J Wuhan Univ Technol-Mat Sci Edit* **30** (2015) 467-472, https://doi.org/10.1007/s11595-015-1173-y

28. V. Ribić *et al*., New inversion boundary structure in Sb-doped ZnO predicted by DFT calculations and confirmed by experimental HRTEM. *Acta Materialia* **199** (2020) 633-648, https://doi.org/10.1016/j.actamat.2020.08.035

29. H. Liu, F. Zeng, Y. Lin, G. Wang, F. Pan, Correlation of oxygen vacancy variations to band gap changes in epitaxial ZnO thin films. *Appl Phys Lett* **102** (2013) 181908, https://doi.org/10.1063/1.4804613

30. S. Haireche, M. Bouchenafa, M. A. Fadla, A. Benmakhlouf, S. Maabed, M. Sidoumou, *Acta Physica Polonica A*, **142** (2022), https://doi.10.12693/APhysPolA.142.216

31. B. B. Nasab, A. Kosarian, N. A. Sheini, Effect of oxygen flow rate in zinc oxide radio frequency magnetron sputtering on the structural and optical properties of ZnO/PEDOT. PSS Inorganic—Organic Hetero-Junction. *Fizika i Tekhnika Poluprovodnikov* **54** (2020) 707, https://doi.10.1134/S1063782620080151

32. V. N. Jafarova, I. C. Scurtu, C. Stanca, N. Acomi and G. Raicu, Defect influence on the electronic and magnetic properties of silver doped (6,0) single-walled ZnO nanotubes: a first-principles study. *Indian J Phys* **98** (2024) 2335-2346, https://doi.org/10.1007/s12648-023-03044-9.

33. Kh. A. Abdullin, M. T. Gabdullin, L. V. Gritsenko, D. V. Ismailov, Zh. K. Kalkozova, S. E. Kumekov, Zh OMukash, A. YuSazonov, E. I. Terukov, Electrical, optical, and photoluminescence properties of ZnO films subjected to thermal annealing and treatment in hydrogen plasma. *Semiconductors* **50** (2016) 1010-1014, https://doi.org/10.1134/S1063782616080029

34. Ma. Tianlei, Effect of precursor concentration and sintering on functional properties of ZnO thin films deposited by aerosol-assisted chemical vapour deposition (AACVD). *Materials Science in Semiconductor Processing* **121** (2021) 105413, https://doi.org/10.1016/j.mssp.2020.105413

35. T. Nachaithong, P. Sikam, P. Moontragoon, T. Kaewmaraya, P. Thongbai, W. Busayaporn, Z. Ikonic, DFT and experimental approaches of effect of (Al, Ga) doping ions on colossal dielectric properties of ZnO ceramic. *Ceramics International* **50** 23 Part C (2024) 52134-52143, https://doi.org/10.1016/j.ceramint.2024.05.336

36. P. Sikam, P. Moontragoon, Z. Ikonic, T. Kaewmaraya, P. Thongbai, The study of structural, morphological and optical properties of (Al, Ga)-doped ZnO: DFT and experimental approaches. *Applied Surface Science* **480** (2019) 621-635, https://doi.org/10.1016/j.apsusc.2019.02.255

37. L. C. Damonte, G. N. Darriba, M. RenterÃa, Structural and electronic properties of Al-doped ZnO semiconductor nanopowders: Interplay between XRD and PALS experiments and first-principles/DFT modeling. *Journal of Alloys and Compounds* **735** (2018) 2471-2478, https://doi.org/10.1016/j.jallcom.2017.11.072

38. G. El Hallani, M. Khuili, N. Fazouan, A. Liba, H. Abou El Makarim, E. H. Atmani, Experimental and DFT investigations of Al-doped ZnO nanostructured thin films. *Chemical Physics Impact* **8** (2024) 100648, https://doi.org/10.1016/j.chphi.2024.100648

39. Y. Larbah, M. Adnane, B. Rahal, Growth and Characterization of ZnO and Al-Doped ZnO Thin Films by a Homemade Spray Pyrolysis. *Semiconductors* **54** (2020) 1439-1444, https://doi.org/10.1134/S1063782620110184

40. I. Jellal, H. Ahmoum, Y. Khaaissa, K. Nouneh, M. Boughrara, M. Fahoume, S. Chopra, J. Naja. Experimental and ab-initio investigation of the microstructure and optoelectronic properties of FCM-CVD-prepared Al-doped ZnO thin films. *Appl Phys A* **125** (2019) 650, https://doi.org/10.1007/s00339-019-2947-4

41. V. Khayrudinov *et al*., Hybrid GaAs nanowire-polymer device on glass: Al-doped ZnO (AZO) as transparent conductive oxide for nanowire-based photovoltaic applications. *Journal of Crystal Growth* **548** (2020) 125840, https://doi.org/10.1016/j.jcrysgro.2020.125840

42. P. Sahoo, C. Tiwari, S. Kukreti, A. Dixit, All oxide lead-free bismuth ferrite perovskite absorber based FTO/ZnO/BiFeO3/Au solar cell with efficiency $\{}sim$ 12%: First principle material and macroscopic device simulation studies. *Journal of Alloys and Compounds* **981** (2024) 173599, https://doi.org/10.1016/j.jallcom.2024.173599

43. W. Kohn , L. J. Sham, Self-consistent equations including exchange and correlation effects. *Phys Rev* **140** (1965) A1133-A1138, https://doi.org/10.1103/PhysRev.140.A1133

44. J. P. Perdew, K. Burke, M. Ernzerhof, Generalized gradient approximation made simple. *Phys Rev Lett* **77** (1996) 3865, https://doi.org/10.1103/PhysRevLett.77.3865

45. M. D. Segall, P. J. D. Lindan, M. J. Probert, C. J. Pickard, P. J. Hasnip, S. J. Clark, First-principles simulation: ideas, illustrations and the CASTEP code. *J Phys Condens Matter* **14** (2002) 2717, https://doi.org/10.1088/0953-8984/14/11/301

46. D. Vanderbilt, Soft self-consistent pseudopotentials in a generalized eigenvalue formalism. *Physical Rev B* **41** (1990) 7892-7895, https://link.aps.org/doi/10.1103/PhysRevB.41.7892

47. S. L. Dudarev, G. A. Botton, S. Y. Savrasov, C. J. Humphreys, A. P. Sutton, Electron-energy-loss spectra and the structural stability of nickel oxide: An LSDA+U study. *Physical Review B.* **57** (1998) 1505-1509, https://link.aps.org/doi/10.1103/PhysRevB.57.1505

48. Q. V. Duong, Investigation of structural and electronic properties of ZnO using first principle calculations. *HPU2 Journal of Science: Natural Sciences and Technology,* **3** (2024) 78-87, https://doi.org/10.56764/hpu2.jos.2024.3.1.78-87

49. V. Anisimov, J. Zaanen, O. K. Andersen, Band theory and Mott insulators: Hubbard U instead of Stoner I. *Physical Review B* **44** (1991) 943, https://doi.org/10.1103/PhysRevB.44.943

50. M. Cococcioni, S. De. Gironcoli, Linear response approach to the calculation of the effective interaction parameters in the LDA U method. *Phys Rev B* **71** (2005) 035105, https://doi.org/10.1103/PhysRevB.71.035105

51. A. Shabani, M. Khazaei Nezhad, N. Rahmani, Y. K. Mishra, B. Sanyal and J. Adam, Revisiting the Optical Dispersion of Aluminum-Doped Zinc Oxide: New Perspectives for Plasmonics and Metamaterials. *Advanced Photonics Research,* **2** (2021), https://doi.org/10.1002/adpr.202000086

52. Vusala Nabi Jafarova, Nazim T Mamedov and Musaver A Musaev, High Curie Temperature and Half-Metallic Ferromagnetism in ZnSe:Co,Ni with Wurtzite Structure: First-Principles Study. *Phys. Status Solidi B,* **260** (2023) 2200360, https://doi.org/10.1002/pssb.202200360

53. Vusala Nabi Jafarova, Structural, electronic and magnetic properties of pure and Fe-doped ZnSe: first-principles investigation. *Pramana - J. Phys.* **98** (2024) 82, https://doi.org/10.1007/s12043-024-02752-z

54. R. Manotum, R. Klinkla, N. Phaisangittisakul, U. Pinsook, T. Bovornratanaraks, Effect of Pressure on the Stability and Electronic Structure of ZnO0.5S0.5 and ZnO0.5Se0.5. *J Electron Mater* **46** (2017) 6856-6863, https://doi.org/10.1007/s11664-017-5708-1

55. L. A. Valdez, M. A. Caravaca, R. A. Casali, Ab-initio study of elastic anisotropy, hardness and volumetric thermal expansion coefficient of ZnO, ZnS, ZnSe in wurtzite and zinc blende phases. *Journal of Physics and Chemistry of Solids* **134** (2019) 245-254, https://doi.org/10.1016/j.jpcs.2019.05.019

56. F. Wang, J. Wu, C. Xia, C. Hu, C. Hu, P. Zhou, L. Shi, Y. Ji, Z. Zheng, X. Liu, Thermodynamic and elastic properties of hexagonal ZnO under high temperature. *J Alloys Compd* **597** (2014) 50-57, https://doi.org/10.1016/j.jallcom.2013.12.212

57. Y. S. Liu, W. Zeng, Z. T. Liu, Q. J. Liu, J. Gao, Z. Jiao, Geometrical, electronic and optical properties of seven types ZnO from first-principles calculation. *Opt Quant Electron* **55** (2023) 1177, https://doi.org/10.1007/s11082-023-05332-4

58. G. Carlotti, D. Fioretto, G. Socino, E. Verona, Brillouin scattering determination of the whole set of elastic constants of a single transparent film of hexagonal symmetry. *J Phys Condens Matter* **7** (1995) 9147-9153, https://doi.org/10.1088/0953-8984/7/48/006

59. M. K. Yaakob, N. H. Hussin, M. F. M. Taib, T. I. T. Kudin, O. H. Hassan, A. M. MAli, M. Z. A. Yahya, First Principles LDA+U Calculations for ZnO Materials. *Integrated Ferroelectrics* **155** (2014) 15-22, http://dx.doi.org/10.1080/10584587.2014.905086

60. R. Moussa, Y. Djalab, M. Maache, R. Khenata, S Bin-Omran, SA Rouf, MW Iqbal, A Abdiche, W. Ahmed, M. Manzour, An investigation using DFT methods on the electronic and optical properties, and mechanical behavior of the wurtzite ZnO1-xTex ternary alloy. *Current Applied Physics* **55** (2023) 82-92, https://doi.org/10.1016/j.cap.2023.09.004

61. K. Meliani, S. Haireche, M. Bouchenafa, M. Elbaa, S. Douakh, R. Chiker, Comprehensive Analysis of the Structural, Electronic, Elastic, and Optical Properties of SrS Compound Under Pressure: First-Principles Calculations. *Braz J Phys* **54** (2024) 46, https://doi.org/10.1007/s13538-024-01419-9

62. M. J. Akhtar, A. H. Alhadlaq, A. Alshamsan, M. A. M. Khan, M. Ahamed, Aluminum doping tunes band gap energy level as well as oxidative stress-mediated cytotoxicity of ZnO nanoparticles in MCF-7 cells. *Sci Rep* **5** (2015) 13876, https://doi.org/10.1038/srep13876

63. P. Anup, S. Heath, D. A. Drabold, Density functional theory model of amorphous zinc oxide (a-ZnO) and a-X0.375Z0.625O (X= Al, Ga and In). *Journal of Non-Crystalline Solids* **455** (2017) 98-101, http://dx.doi.org/10.1016/j.jnoncrysol.2016.10.035

64. S. Haireche, A. Benmakhlouf, M. Bouchenafa, S. Maabed, M. Bouhamida, M. Sidoumou, First principles study of structural and electronic properties of binary strontium chalcogenides under pressure. *Sigma J Eng Nat Sci* **41** (2023) 1231-1242, http://dx.doi.org/10.14744/sigma.2023.00142

65. N. Kamarulzaman, M. F. Kasim, R. Rusdi, Band Gap Narrowing and Widening of ZnO nanostructures and doped materials. *Nanoscale Res Lett* **10** (2015) 346, https://doi.org/10.1186/s11671-015-1034-9

66. G. C. Zhou, L. Z. Sun, X. L. Zhong, X. Chen, Lu Wei, J. B. Wang, First-principle study on bonding mechanism of ZnO by LDA+U method. *Physics Letters A* **368** 1-2 (2007) 112-116, https://doi.org/10.1016/j.physleta.2007.03.061

67. M. Khuili, N. Fazouan, H. Abou El Makarim, G. El Halani, E. H. Atmani, Comparative first principles study of ZnO doped with group III elements. *Journal of Alloys and Compounds* **688 Part B** (2016) 368-375, https://doi.org/10.1016/j.jallcom.2016.06.294

68. A. Jemmy Cinthia, G. Sudhapriyang, R. Rajeswarapalanichamy, M. Santhosh, Structural, electronic and elastic properties of ZnO and CdO: A first-principles study. *Procedia Materials Science* **5** (2014) 1034-1042, https://doi.org/10.1016/j.mspro.2014.07.394

69. F. Mouhat, F. X. Coudert, Necessary and sufficient elastic stability conditions in various crystal systems. *Physical Review B* **90** (2014) 224104, https://link.aps.org/doi/10.1103/PhysRevB.90.224104

70. J. Wang, J. Li, S. Yip, S. Phillpot, D. Wolf, Mechanical instabilities of homogeneous crystals. *Phys Rev B* **52** (1995) 12627, https://link.aps.org/doi/10.1103/PhysRevB.52.12627

71. O. H. Nielsen and R. M. Martin, First-principles calculation of stress. *Physical Review B* **32** (1985) 3780-3791, https://doi.org/10.1103/PhysRevB.32.3780

72. F. Silvearv, A. L. Rosa, S. Lebègue, R. Ahuja, An ab-initio study of (Mn,Al) doped ZnO including strong correlation effects. *Physica E: Low-dimensional Systems and Nanostructures* **44** (2012) 1095-1097, https://doi.org/10.1016/j.physe.2010.12.007.

73. R. Manotum, R. Klinkla, N. Phaisangittisakul, U. Pinsook, K.Bovornratanaraks, Effect of pressure on the stability and electronic structure of ZnO0.5S0.5 and ZnO0.5Se0.5. *J Electron Mater* **46** (2017) 6856-6863, https://doi.org/10.1007/s11664-017-5708-1

74. G. Carlotti, D. Fioretto, G. Socino, E. Verona, Brillouin scattering determination of the whole set of elastic constants of a single transparent film of hexagonal symmetry. *Journal of Physics: Condensed Matter* **7** (1995) 9147-9153, urlhttps://doi.org/10.1088/0953-8984/7/48/006

75. B. Huang, Doping of RE ions in the 2D ZnO layered system to achieve low-dimensional upconverted persistent luminescence based on asymmetric doping in ZnO systems. *Physical Chemistry Chemical Physics* **19** (2017) 12683-12711, https://doi.org/10.1039/C7CP01623A

76. MV. SA. Rosely, DR. A. Luisa, F. Thomas, S. DA. Jailton, Optoelectronic Properties of Zinc Oxide: A First-Principles Investigation Using the Tran-Blaha Modified Becke-Johnson Potential. *Physica Status Solidi (b)* **256** (2019) 4, http://dx.doi.org/10.1002/pssb.201800380

77. S. Haireche, S. Douakh, M. Elbaa, M. Bouchenafa, K. Meliani, Influence of phase transition on the mechanical and optical properties of SrSe and SrTe compounds via ab initio calculations. *Physica B* **696** (2025) 416610, https://doi.org/10.1016/j.physb.2024.416610

78. D. Dada, M. DA. Mochena, DFT+U Study of Absorption Spectra and Localized Surface Plasmon Resonances of few electrons in Doped ZnO Quantum Dots. *Cond Mat Mtrl-sci*. (2023), https://arxiv.org/abs/2401.00074

79. M. Khuili, N. Fazouan, H. Abou El Makarim, E. H. Atmani, P. RaiD, M. Houmad, DFT study of rare earth (Tm, Yb, Ce) doped ZnO: structural, optoelectronic and electrical properties. *Cond Mat Mtrl-sci*. (2020), https://arxiv.org/abs/2004.10728

80. A. G. Alharshan, A. M. Aboraia, Uosif AM, Sharaf MI, Shaaban RE, Saad M, ALMohiy H, Elsenety MM Optical Band Gap Tuning, DFT Understandings, and Photocatalysis Performance of ZnO Nanoparticle-Doped Fe Compounds. *Materials* **16** (2023) 2676, https://doi.org/10.3390/ma16072676

81. W. M. Murphy, R. W. Diebel, Y. M. Yiu, T. K. Sham, Cr doped ZnO nanostructures: synthesis, electronic structures, and magnetic properties. *Canadian Journal of Chemistry* **95** (2017), https://doi.org/10.1139/cjc-2017-0143

82. M. Irungu, S. Kiprotich, M. M. Winfred, A DFT Investigation of RE (Ce, Dy, Eu) Doped Monolayer ZnO for Potential Application in Dye Sensitized Solar Cells Application. *Nanoscience and Nanotechnology* **13** (2024) 17-27, https://doi.org/10.5923/j.nn.20241302.01

83. J. Tauc, R. Grigorovici and A. Vancu, Optical Properties and Electronic Structure of Amorphous Germanium. *Physica Status Solidi (b)*, **15** (1966) 627-637, https://doi.org/10.1002/pssb.19660150224